

Correspondence and requests for materials should be addressed to jianwangphysics@pku.edu.cn (J.W.), xcxie@pku.edu.cn (X.C.X.), gwljiashuang@pku.edu.cn (S.J.).

Anomalous Quantum Oscillations in 3D Dirac Semimetal Cd_3As_2 Induced by 3D Nested Anisotropic Fermi Surface

Yanfei Zhao^{1,2,#}, Haiwen Liu^{1,2,#}, Chenglong Zhang^{1,2}, Huichao Wang^{1,2}, Junfeng Wang³, Ziquan Lin³, Ying Xing^{1,2}, Hong Lu^{1,2}, Jun Liu⁴, Yong Wang⁴, Shuang Jia^{1,2,*}, X. C. Xie^{1,2,*} and Jian Wang^{1,2,*}

¹International Center for Quantum Materials, School of Physics, Peking University, Beijing 100871, China

²Collaborative Innovation Center of Quantum Matter, Beijing 100871, China

³Wuhan National High Magnetic Field Center, Huazhong University of Science and Technology, Wuhan 430074, China

⁴Center of Electron Microscopy, State Key Laboratory of Silicon Materials, Department of Materials Science and Engineering, Zhejiang University, Hangzhou, 310027, China

[#] Authors equally contributed to this work.

ABSTRACT

The three-dimensional (3D) topological Dirac semimetal is a new topological phase of matter, viewed as the 3D analogy of graphene with a linear dispersion in the 3D momentum space. Here, we report the angular dependent magnetotransport in Cd_3As_2 single crystal and clearly show how the Fermi surface evolves when tilting the magnetic field. Remarkably, when the magnetic field lies in $[112]$ and $[11\bar{1}]$ axis, only single oscillation period features present, however, the system shows double period oscillations when the field is applied along $[1\bar{1}0]$ direction. Moreover, tilting the magnetic field at certain direction also gives double period oscillations. We attribute the anomalous oscillation behavior to the sophisticated geometry of Fermi surface and illustrate a complete 3D Fermi surfaces with two nested anisotropic ellipsoids around the Dirac point. Additionally, a sub-millimeter mean free path at 6 K is observed in Cd_3As_2 crystal, indicating a large ballistic transport region in this material. These results improve the knowledge of the Dirac semimetal material Cd_3As_2 , and also pave the way for proposing new electronic applications based on 3D Dirac materials.

The three-dimensional (3D) topological Dirac semimetal, a new type of topological materials

with a pair of nondegenerate 3D massless Weyl fermions becomes a rapid growing field of research in condensed matter physics¹⁻¹³. In analogy to two dimensional Dirac points observed in graphene¹⁴ and topological insulators¹⁵⁻¹⁹, 3D Dirac semimetal possesses bulk Dirac fermions with linear dispersion along three momentum directions²⁰.

Motivated by theoretical predications^{1,2}, to date, Na_3Bi ³ and Cd_3As_2 ^{4,5,10,21} have been identified to be 3D topological Dirac semimetal by angle resolved photoemission spectroscopy (ARPES). More recently, scanning tunneling microscopy (STM) experiments have revealed quasiparticle interference and the extended Dirac-like dispersion in Cd_3As_2 ⁶. This unusual band dispersion also makes the electrons around the Fermi surface behave many unusual transport phenomena such as strong quantum oscillations⁸, ultrahigh mobility⁹ and large magnetoresistance^{9,12}. However, most magnetotransport measurements have been limited to study the quantum oscillations in one direction or by rotating the magnetic field only in one plane. The scarcity of the complete 3D Fermi surface analysis hinders an in-depth understanding of the physical properties in Cd_3As_2 single crystal. Therefore, it is highly desirable to demonstrate the transport property study at different magnetic field direction as well as the angular dependent magnetotransport to reveal the complicated 3D Fermi surface in Cd_3As_2 system.

Here, we present a systematic study of the magnetotransport in Cd_3As_2 single crystal and firstly extend our study to the angular dependence of magnetoresistance in three independent directions as well as the high magnetic field experiments (up to 54 T). The SdH oscillations signified a previously unknown Fermi surface with two nested ellipsoids, leading to a good understanding on its 3D Dirac nature and also providing a platform to explore exotic physical phenomena.

Results

Sample Structure. Single crystal of Cd_3As_2 are synthesized from a Cd-rich melt with the stoichiometry Cd_8As_3 in the evacuated quartz ampoule²². The Cd_3As_2 single crystal is examined by a FEI TITAN Cs-corrected cross sectional scanning transmission electron microscopy (STEM) operating at 200kV. Figure 1a shows the atomic layer by layer high angle annular dark field scanning transmission electron microscopy (HAADF-STEM) image which manifests a high quality single crystal nature of Cd_3As_2 sample. An optical image of the measured sample is shown in the inset of Figure 1d. The crystal is needle-like and grows preferentially along the $[1\bar{1}0]$ direction (the length direction). The width direction is along $[11\bar{1}]$ and the largest facet of the crystal is (112) plane. Standard four probe method is used to measure the Cd_3As_2 samples on its (112) plane. Two indium current electrodes (I+ and I-) are pressed on both ends and across the entire width of the sample, so that the current can homogeneously go through the sample in the length direction $[1\bar{1}0]$. The other two indium electrodes were pressed on the crystal as voltage probes. Angular dependence of magnetoresistance was measured by rotating the sample in $(1\bar{1}0)$

plane and (112) plane, characterized by the angle θ and φ illustrated in Figure 1b, respectively. The transport measurements were carried out in a PPMS-16T system (Quantum Design) and pulsed high magnetic field at Wuhan National High Magnetic Field Center.

Transport Properties. More than ten samples have been studied. Data presented here are from two typical samples: Sample 1 and 2. Figure 1c shows the resistivity of sample 1 as a function of temperature (T). The resistivity decreases almost linearly when T decreases from 300 K to about 6 K and then tends to be saturated. It displays a perfect linear metallic property with a large residual resistivity ratio $RRR = 2120$ (the resistivity at room temperature over the resistivity at 6 K). As shown in the insert panel of Figure 1c, the resistivity ρ is quite low (about $11.6 \text{ n}\Omega \cdot \text{cm}$ at 6 K). Similar results have been reported before⁹, suggesting the behavior is related to its long transport lifetime. More interestingly, when T is lower than 6 K, the resistivity oscillates near zero resistivity within the resolution of our measurement instrument (about $4.5 \text{ n}\Omega \cdot \text{cm}$), which could be understood in terms of the quantum ballistic transport. Estimated from the Shubnikov-de Haas (SdH) oscillations of sample 1, the carrier density is about $5.86 \times 10^{18} \text{ cm}^{-3}$ (Supplementary Information). It is worth noting that the carrier density estimation from SdH might be two to ten times smaller than the carrier density in Hall measurement⁹. Therefore, the mobility is estimated to be $9.19 \times 10^6 \sim 4.60 \times 10^7 \text{ cm}^2/\text{Vs}$ and the mean free path l_0 is about $0.25 \sim 1.25 \text{ mm}$ at 6 K, which are consistent with the previous transport study⁹. The high mobility and long mean free path shed new light on realizing various applications on high frequency topological functional devices. Additionally, the linear metallic $\rho - T$ behavior is also observed in other samples, such as sample 2 shown in Figure 1d.

To investigate the 3D shapes of Fermi surfaces of Cd_3As_2 , the analysis of SdH oscillations measured in three independent magnetic field directions, along $[112]$, $[11\bar{1}]$ and $[1\bar{1}0]$ axes ($B_{[112]}$, $B_{[11\bar{1}]}$ and $B_{[1\bar{1}0]}$) are shown in Figure 2. Figure 2a to c displays the field dependencies of resistivity measured in three magnetic fields at different temperatures. Pronounced SdH oscillations are clearly visible around 4 T up to 50 K, and then diminished at higher temperatures for all field directions. After subtracting a fourth-order polynomial background, the oscillatory component $\Delta\rho$ in three field directions are plotted in Figure 2d to f, respectively. The frequency of the SdH oscillations was extracted from the fast Fourier transform (FFT) analysis. Only one fundamental frequency is observed in both $B_{[112]}$ and $B_{[11\bar{1}]}$ directions with the period $B_{F[112]} = 54.30 \text{ T}$ and $B_{F[11\bar{1}]} = 43.44 \text{ T}$, indicating a relatively simple but anisotropic Fermi surface in the two directions and the Fermi surface in $B_{[11\bar{1}]}$ direction is smaller than that measured in $B_{[112]}$ direction. Interestingly, Figure 2f illustrates a different set of SdH oscillations when the magnetic field is applied parallel to $[1\bar{1}0]$ axis. Compared with the magnetoresistance measured along $[112]$ and $[11\bar{1}]$ direction, the

SdH oscillations in $B_{[1\bar{1}0]}$ direction are obviously weaker and nonperiodic. At around 8 T, the oscillation seems to be suppressed and then appears again at about 10 T. The inset of Figure 2f shows the FFT of SdH oscillations in $B_{[1\bar{1}0]}$ direction, two well-defined peaks appears at $F_1 = 43.44$ T and $F_2 = 54.30$ T. According to the Onsager relation, the frequency of the magnetoresistance oscillation is related to the external cross-sectional area A_k of the Fermi surface in the momentum space: $F = \frac{\hbar}{2\pi e} A_k$, thus, gives two cross-sectional areas of Fermi surface perpendicular to the field $A_{F1} = 4.17 \times 10^{-3} \text{ \AA}^{-2}$ and $A_{F2} = 5.18 \times 10^{-3} \text{ \AA}^{-2}$, indicating a complicated Fermi surface.

In order to verify and analyze the SdH oscillations, we fit the entire oscillatory component with the standard Lifshitz–Kosevich (LK) theory for a 3D system²³⁻²⁵

$$\Delta\rho \propto \frac{\lambda}{\sinh \lambda} e^{-\lambda_D} \cos 2\pi \left[\frac{F}{B} + \gamma - \delta \right] \quad (1)$$

with $\lambda = 2\pi^2 k_B T m^* / \hbar e B$ and $\lambda_D = 2\pi^2 k_B T_D m^* / \hbar e B$, where m^* is the cyclotron effective mass of the carriers and T_D is the Dingle temperature. γ is the phase related to the berry phase while δ is a phase shift determined by the dimensionality, taking the value $\delta = \pm 1/8$ for 3D system²⁴. Considering the two frequencies obtained in $B_{[1\bar{1}0]}$ direction, we use two independent parameters F_1 and F_2 to fit the oscillation. As shown by the red solid line in Figure 2f, fitting to the LK theory yields two frequencies $F_1 = 44.37$ T and $F_2 = 52.85$ T. The two frequencies almost consistent with the FFT results $F_1 = 43.44$ T and $F_2 = 54.30$ T, confirming the complex physics in this direction. On the other hand, the LK theory fitting to the oscillations in $B_{[112]}$ and $B_{[11\bar{1}]}$ directions with a single frequency are shown in the supplementary information. The fitting to the oscillation in $B_{[112]}$ direction yields $F_{[112]} = 54.13$ T, $T_D = 36.93 \pm 1.5$ K, and $\gamma - \delta = 0.3$, respectively. For the $B_{[11\bar{1}]}$ case, the good fitting gives $F_{[11\bar{1}]} = 42.6$ T, $T_D = 33.54 \pm 2.5$ K, and $\gamma - \delta = 0.2$. Both of the fitting results are consistent with the frequency identified from FFT spectra ($F_{[112]} = 54.30$ T and $F_{[11\bar{1}]} = 43.44$ T). From the temperature dependence of the oscillation amplitude (Fig. 2d and 2e), we obtain the cyclotron effective mass $m_{[112]}^* = 0.043 m_e$ and $m_{[11\bar{1}]}^* = 0.036 m_e$ (m_e is the free electron mass). Therefore, taking into account all three different directions, the observed periods point to a 3D Fermi surface is a simple anisotropic ellipse along both $[112]$ and $[11\bar{1}]$ direction, while, with complicated geometry along $[1\bar{1}0]$ axis.

Moreover, to further understand the anisotropic 3D Fermi surface, the analysis of nontrivial Berry phase deduced from SdH oscillations is necessary. The Landau Level fan diagram of $B_{[112]}$ direction is plotted in Figure 3a. The maxima of ρ are assigned to be the integer indices (solid circles) while the minima of ρ are plotted by open circles in the diagram as half integer indices²⁴. A linear extrapolation of the index plot gives the intercept value close to 0.3. Considering the study before²⁴, in a 3D system, the intercept of the index plot should be $0 \pm 1/8$ (+ for holes and – for electrons). In our system, the intercept is 0.3, deviating from $\pm 1/8$, indicating the Fermi surface is an anisotropic ellipsoid instead of spherical with perfect π Berry phase. Similarly, the LL fan diagram in $B_{[1\bar{1}0]}$ direction is shown in Figure 3b. As discussed previously, the intercept value obtained is about 0.2, different from 0.3 yielded in $B_{[112]}$ direction, also consistent with the assumption of the anisotropic Fermi surface in Cd_3As_2 system. Figure 3c displays the magnetoresistance behavior measured in pulsed high magnetic field normal to the (112) plane up to 54 T at various temperatures. The larger and more obvious SdH oscillations in high field provide an opportunity to study the further physics in the quantum limit. However, limited by the measurement resolution, the small oscillations in the lower field is hard to distinguish from noise. A similar plot based on the maxima and minima of ρ versus the index n are shown in Figure 3d. The intercept shifts to 0.38 instead of 0.3 deduced from the relatively low magnetic field. It suggests that the high magnetic field is needed to fix the intercept more reliable.

To study the 3D Fermi surface of Cd_3As_2 systematically, the angular dependence of SdH oscillations are important to show the evolution of Fermi surface changing in different directions. Figure 4a shows the angular dependent oscillations after removing the polynomial background for the transverse rotation ($B \perp I$) by varying magnetic field angle θ tilting from perpendicular field ($B_{[112]}$) to parallel field ($B_{[11\bar{1}]}$). θ is the angle between magnetic field and $[112]$ axis. Figure 4b shows the angular-dependent SdH oscillations for the transverse to longitudinal rotation in (112) plane (I was applied along $[1\bar{1}0]$ and B was rotated from $[11\bar{1}]$ towards $[1\bar{1}0]$). ϕ is the angle between magnetic field and $[11\bar{1}]$ axis. As shown in Table I, the FFT analysis gives out when the magnetic field lies in $[112]$ and $[11\bar{1}]$ axis, only one period features present, however, the system shows double period oscillations when the field applied along $[1\bar{1}0]$ axis. Moreover, when changing the magnetic field angle θ , two period oscillations also present. We attribute these anomalous SdH oscillations to the sophisticated geometry of Fermi surface.

Discussion

From pervious theoretical and experimental results^{2,4}, the Fermi surface is two anisotropic ellipsoids around the Dirac point, with Fermi momentum k_z much larger than k_x and k_y . Moreover,

when the Fermi energy goes beyond the Lifshitz saddle point, these two separate ellipsoids finally change into two nested ellipsoids. Therefore, the anomalous two-period SdH oscillations in $B_{[1\bar{1}0]}$ direction maybe essentially originate from these two nested ellipsoid Fermi surface, as shown in Figure 5c.

To further analysis the nested ellipsoid Fermi surface beyond the Lifshitz saddle point, we calculate the Fermi wave vectors at different directions. Based on the SdH period $S_{F[112]} = 54.30$ T and $S_{F[11\bar{1}]} = 43.44$ T for $B_{[112]}$ and $B_{[11\bar{1}]}$ direction, we obtained the mean momentum $k_{[112]} = 0.041$

\AA^{-1} and $k_{[11\bar{1}]} = 0.036 \text{ \AA}^{-1}$, implying an anisotropic rather than a spherical Fermi surface, which is qualitatively consistent with ARPES results⁴. Next, we analysis the anomalous SdH oscillations observed in the angular dependent measurements shown in Table I. This anomalous SdH oscillation can be attributed to the nested ellipsoid Fermi surface beyond the Lifshitz saddle point.

Firstly, for the $B_{[112]}$ and $B_{[11\bar{1}]}$ direction, the maximum cross-section of Fermi surface does not pass through the nested region (see Fig. 5a and b), thus, giving only single period. When the magnetic field is twisted from $[112]$ to $[11\bar{1}]$, the maximum cross-sections of Fermi surface penetrate into the nested region at certain angle range, and form two nested ellipses as shown in Figure 5d. Secondly, when magnetic field is twisted from $[11\bar{1}]$ to $[1\bar{1}0]$, the maximum cross-section of Fermi surface also form two nested ellipses when the direction of magnetic field is around $[1\bar{1}0]$ direction(see Fig. 5c and d). The two nested ellipses lead to the anomalous two-period SdH oscillaitons in Table I. As shown in Figure 5d, the small dashed (red or blue) ellipse leads to the unchanged period $F_1 = 43.44$ T, while the overlapping region changes all the time, corresponding to the varied period F_2 shown in Table I. Therefore, the geometry of maximum cross-sections in Fermi surface can qualitatively interpret the anomalous SdH oscillations when tilting the magnetic field angle. (See the Supplementary Information for further analysis.)

From the above analysis, we know that the Fermi energy is above the Lifshitz saddle point and the Fermi surface merged in certain momentum region. Thus, the topological correction from all two Dirac point contribute to the Landau level intercept value, which makes the intercept value deviates from the theoretical value of $-1/8$ for electron type and results in different intercept values for different magnetic field orientations, which is consistent with the STM results⁶. In addition, comparing the Fermi surface with the previous reported Wigner-Seitz unit cell², we conclude that the Fermi surface in Cd_3As_2 is very large. Due to this large Fermi surface, the Umklapp relation²⁷ can be satisfied and the Umklapp electron-phonon scattering processes plays dominant role on the resistivity at low temperature in Cd_3As_2 , which leads to $R \sim T \cdot N_{\text{ph}}$ with N_{ph}

denoting the number of phonons that satisfies the Umklapp relation²⁷. Moreover, due to the ultra-large unit cell of Cd₃As₂, low energy optical phonon modes might exist in the system. Therefore, the Umklapp processes and optical phonon modes can lead to almost linear R-T relation down to very low temperature, and the observed linear R-T behavior in Figure 1c and d deviates from the ordinary Bloch-Grüneisen Law with $R \sim T^5$ and the electron-electron interaction induced $R \sim T^2$ law²⁷.

In summary, we firstly report pronounced SdH oscillations measured along three different directions in high quality Cd₃As₂ single crystals, and extend our study to the angular dependent magnetotransport and in the high magnetic field close to the quantum limit. By analyzing the SdH oscillations in different magnetic field orientation, we obtain a complete 3D Fermi surface with two nested ellipsoids. Furthermore, we present the changing of the angular-dependent oscillation periods are essentially due to the complicated nested 3D Fermi surface. In addition, the sub-millimeter scale mean free path and ballistic transport region have been demonstrated in Cd₃As₂ single crystal. These results intensify the previous knowledge of the Dirac semimetal material Cd₃As₂, offer a better understanding of existing 3D Dirac semimetals, and reveal the potential of application in topological electronic devices.

Methods

Sample growth. Single crystals of Cd₃As₂ were grown from a Cd-rich melt with the ratio of Cd:As = 85:15. High purity elements (99.99%) were sealed in an evacuated quartz ampoule. The ampoule was heated up to 825°C and kept there for 48 hours. Then it was cooled down to 425°C at a rate of 6 °C/hr. The remaining liquid was decanted at this temperature. The single crystals of Cd₃As₂ crystallized in a needle-like form with metallic luster.

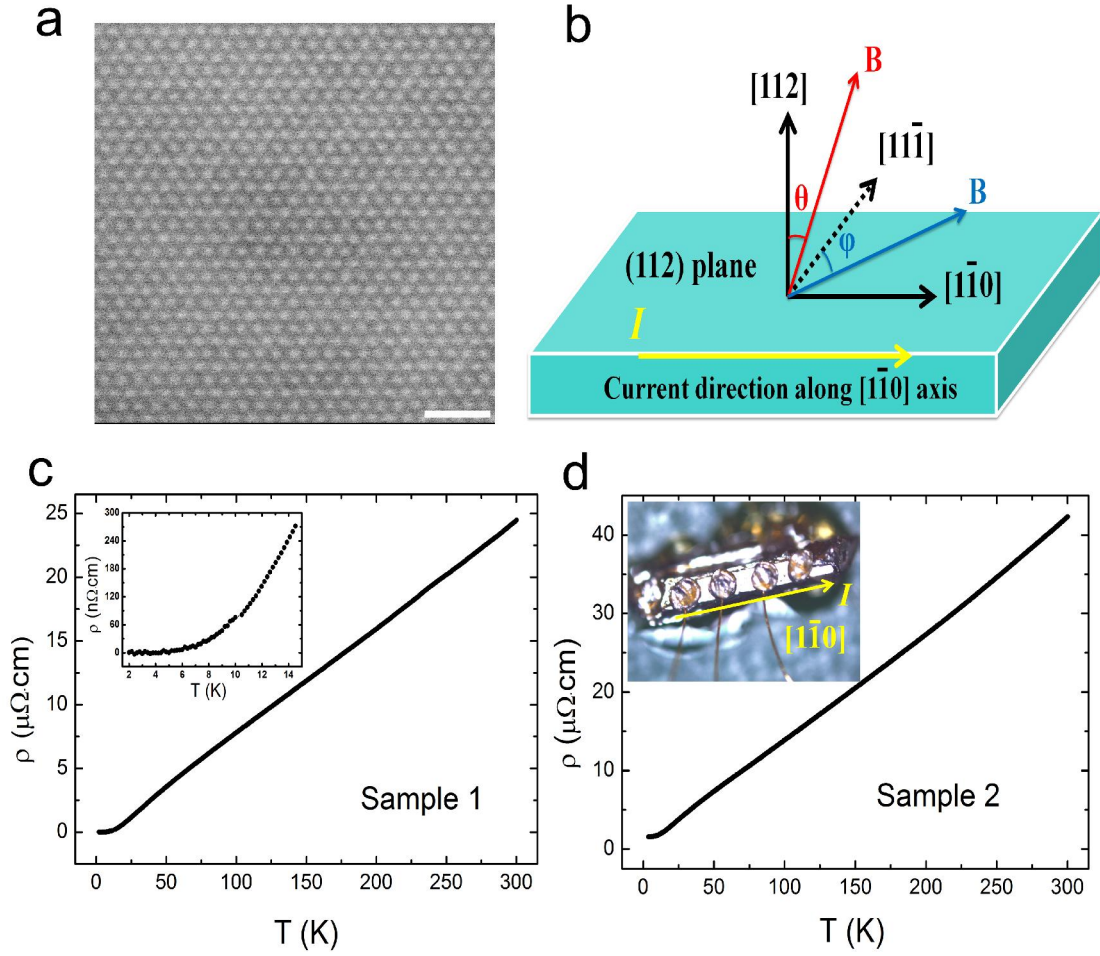


Figure 1: Sample structure of Cd₃As₂ single crystal. (a) High angle annular dark field scanning transmission electron microscopy (HAADF-STEM) image of Cd₃As₂ single crystal. Scale bar represents 1nm. (b) Schematic structure for the angular dependent magnetotransport measurements in Cd₃As₂ system. Sample is rotated in (110) plane and (112) plane, characterized by the angle θ and ϕ , respectively. The sample size is not to scale. (c) Resistivity of sample 1 as a function of temperature. The inset shows the resistivity falling to quite low value about $11.6\text{ n}\Omega\cdot\text{cm}$ at 6K and then oscillating near zero resistivity. (d) ρ (T) behavior of Sample 2. The inset shows an optical image of the measured Cd₃As₂ sample. Standard four probe method is used to measure the transport property.

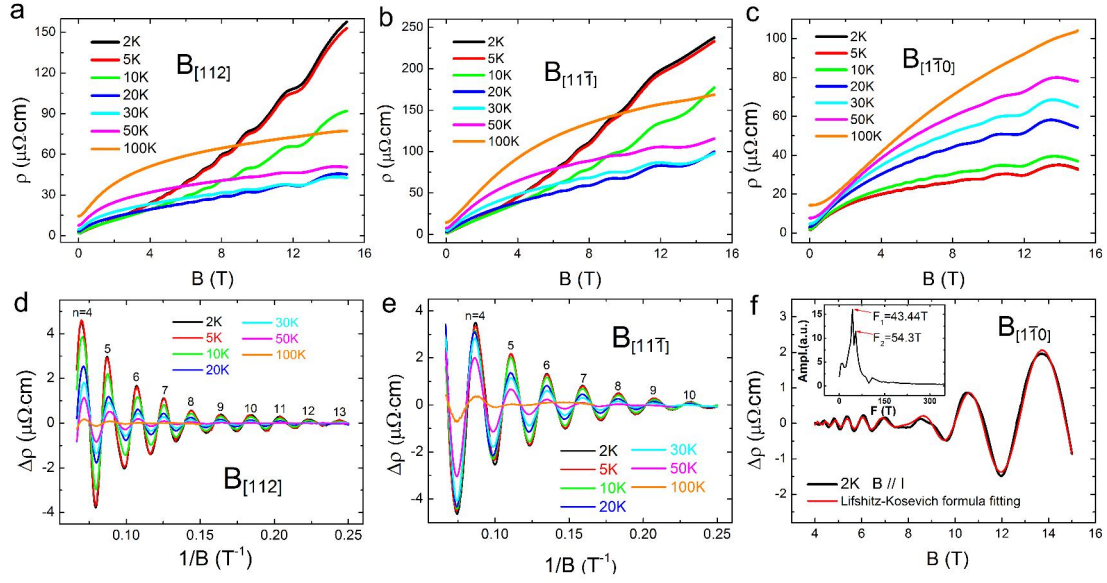


Figure 2: SdH oscillations for Cd₃As₂ single crystal in different magnetic field directions, along the $[112]$, $[11\bar{1}]$ and $[1\bar{1}0]$ axes ($B_{[112]}$, $B_{[11\bar{1}]}$ and $B_{[1\bar{1}0]}$). (a)-(c) Magnetoresistivity measured in the perpendicular field $B_{[112]}$, the parallel field $B_{[11\bar{1}]}$ and $B_{[1\bar{1}0]}$ at different temperatures, respectively. (d)-(e) The oscillatory component of $\Delta\rho$ extracted from ρ by subtracting a forth-polynomial background, as a function of $1/B$ at varies temperatures in $B_{[112]}$ and $B_{[11\bar{1}]}$ directions. (f) The LK theory fitting to the $\Delta\rho$ (B) curve measured at $T = 2$ K in the parallel field $B_{[1\bar{1}0]}$ with two frequencies. (red solid curve). Inset shows the FFT analysis with two frequencies in $B_{[1\bar{1}0]}$ direction.

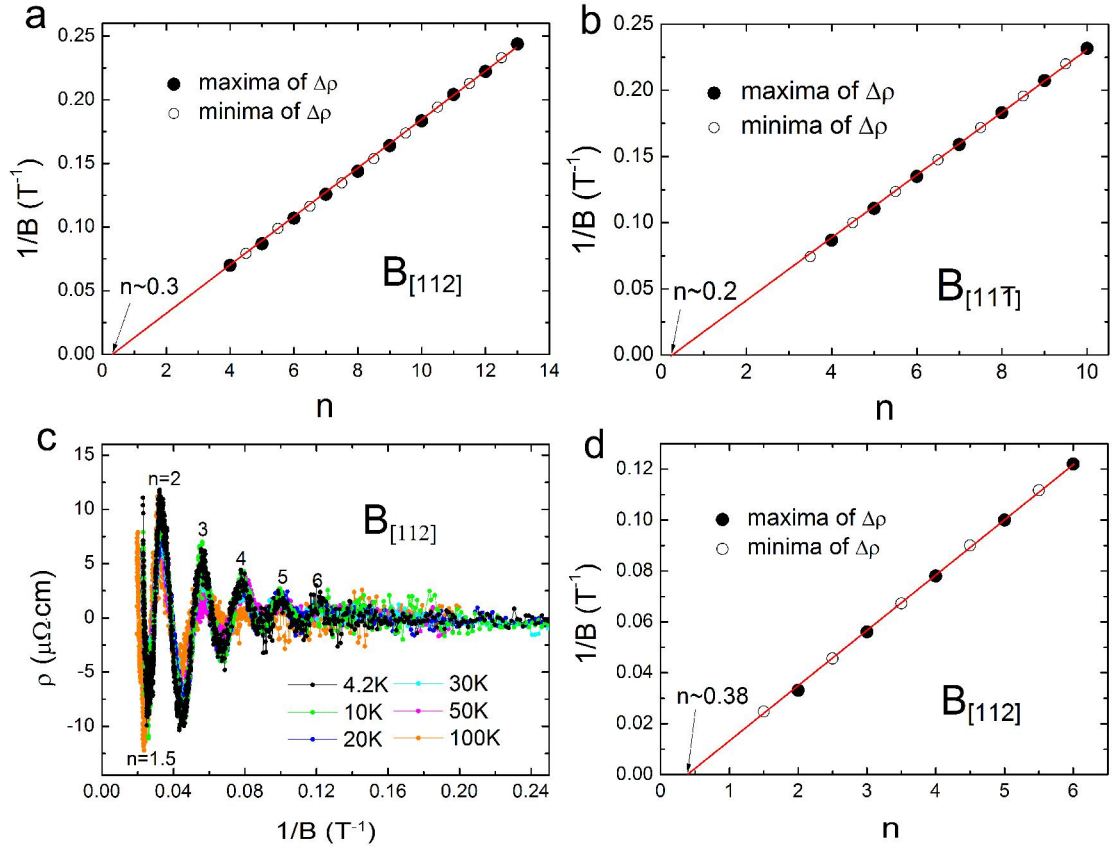


Figure 3 Landau level index plots for Cd₃As₂ single crystal in $B_{[112]}$ and $B_{[111]}$ directions. (a) Landau level index plot of the Fermi surface in the perpendicular field $B_{[112]}$. The maxima of $\Delta\rho$ are assigned to be the integer indices (solid circles) while the minima of $\Delta\rho$ are plotted by open circles as half integer indices. The intercept is close to 0.3. **(b)** Landau level plot for oscillations in $\Delta\rho$ measured at 2 K in the parallel field $B_{[111]}$. Solid line is a linear fitting to the data, giving the intercept about 0.2. **(c)** SdH oscillations measured in the PHMF in the perpendicular field $B_{[112]}$. **(d)** shows the index plot of $1/B$ versus n measured in pulsed high magnetic field. The intercept is about 0.38.

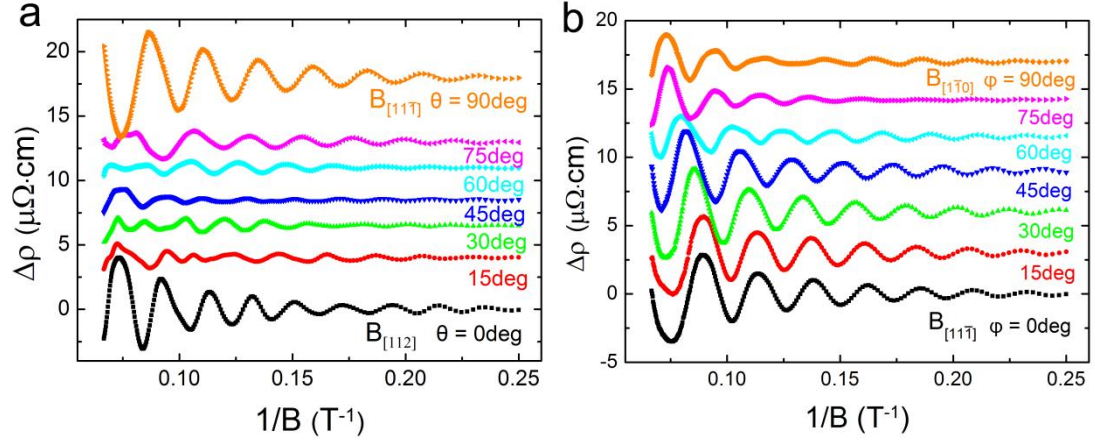


Figure 4 Angular dependent of SdH oscillations at different magnetic field directions. (a) SdH oscillations in $\Delta\rho$ for various magnetic field angles from $B_{[112]}$ ($\theta = 0^\circ$, B in the $[112]$ direction) to $B_{[11\bar{1}]}$ ($\theta = 90^\circ$, B in the $[11\bar{1}]$ direction). (b) SdH oscillations rotates from $B_{[11\bar{1}]}$ ($\phi = 0^\circ$, B in the $[11\bar{1}]$ direction) to $B_{[1\bar{1}0]}$ ($\phi = 90^\circ$, B in the $[1\bar{1}0]$ direction). Figure 1b depicts the definition of θ and ϕ .

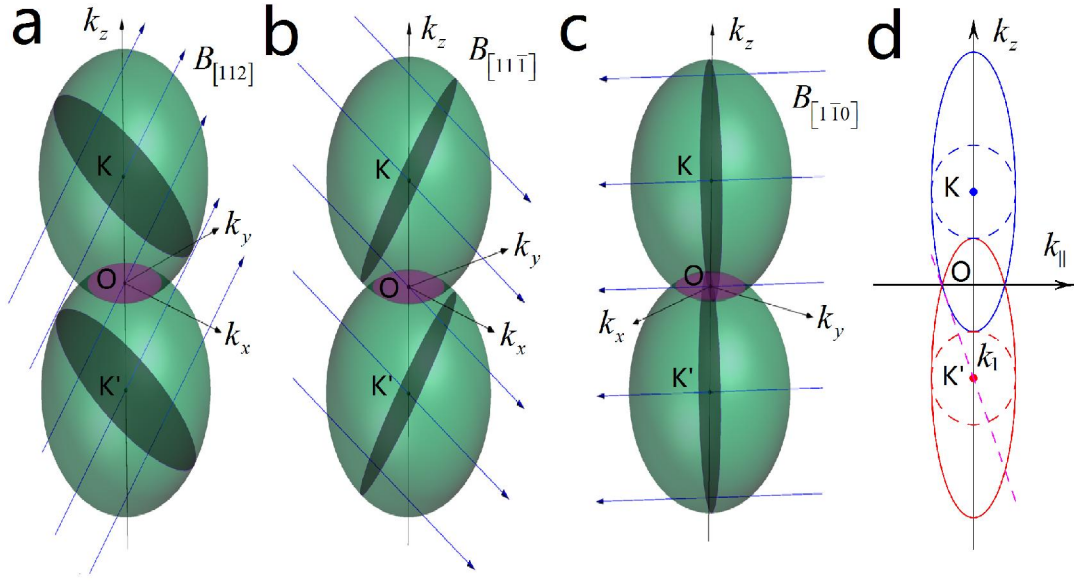


Figure 5 Theoretical analysis of 3D Nested Anisotropic Fermi Surface in Cd_3As_2 . (a)-(c) show the largest cross section of Fermi surface versus the magnetic field orientation. The Fermi surface is two nested anisotropic ellipsoids. (d) shows the schematic plot of the Fermi surface for $B_{[1\bar{1}0]}$ with an overlapping region. The figures are not drawn to scale.

Table I

FFT analysis of SdH oscillations in various magnetic field directions							
$B_{[112]}$ rotate to $B_{[11\bar{1}]}$	0 deg $B_{[112]}$	15 deg	30 deg	45 deg	60 deg	75 deg	90 deg $B_{[11\bar{1}]}$
	54.30 T	43.44 T 54.30 T	48.87 T 59.73 T	54.30 T	48.87 T	43.44 T	43.44 T
$B_{[11\bar{1}]}$ rotate to $B_{[1\bar{1}0]}$	0 deg $B_{[11\bar{1}]}$	15 deg	30 deg	45 deg	60 deg	75 deg	90 deg $B_{[1\bar{1}0]}$
	43.44 T	43.44 T	43.44 T	43.44 T	43.44 T 48.87 T	48.87 T 43.44 T	43.44 T 54.30 T

References

1. Wang, Z. *et al.* Dirac semimetal and topological phase transitions in A_3Bi ($A = Na, K, Rb$). *Phys. Rev. B* **85**, 195320 (2012).
2. Wang, Z., Weng, H., Wu, Q., Dai, X. & Fang, Z. Three-dimensional Dirac semimetal and quantum transport in Cd_3As_2 . *Phys. Rev. B* **88**, 125427 (2013).
3. Liu, Z. K. *et al.* Discovery of a Three-Dimensional Topological Dirac Semimetal, Na_3Bi . *Science* **343**, 864-867 (2014).
4. Liu, Z. K. *et al.* A stable three-dimensional topological Dirac semimetal Cd_3As_2 . *Nat. Mater.* **13**, 677-681 (2014).
5. Neupane, M. *et al.* Observation of a three-dimensional topological Dirac semimetal phase in high-mobility Cd_3As_2 . *Nat. Commun.* **5**, 3786 (2014).
6. Jeon, S. *et al.* Landau quantization and quasiparticle interference in the three-dimensional Dirac semimetal Cd_3As_2 . *Nat. Mater.* **13**, 851-856 (2014).
7. Zhu, Z. & Hoffman, J. E. Condensed-matter physics: Catching relativistic electrons. *Nature* **513**, 319-320 (2014).
8. He, L. P., Hong, X. C., Dong, J. K., Pan, J., Zhang, Z., Zhang, J. & Li, S. Y. Quantum transport in the three-dimensional Dirac semimetal Cd_3As_2 . Preprint at <http://arXiv.org/abs/1404.2557> (2014).
9. Tian, L., Gibson, Q., Ali, M. N., Liu, M., Cava, R. J., and Ong, N. P. Ultrahigh mobility and giant magnetoresistance in Cd_3As_2 : protection from backscattering in a Dirac semimetal. Preprint at <http://arXiv.org/abs/1404.7794> (2014); *Nat. Mater.* doi: 10.1038/NMAT4143 (2014).
10. Borisenko, S., Gibson, Q., Evtushinsky, D., Zabolotnyy, V., Büchner, B. & Cava, R. J. Experimental Realization of a Three-Dimensional Dirac Semimetal. *Phys. Rev. Lett.* **113**, 027603 (2014).
11. Gibson, Q. D., Schoop, L. M., Muechler, L., Xie, L. S., Hirschberger, M., Ong, N. P., Car, R. & Cava, R. J. 3D Dirac semimetals: current materials, design principles and predictions of new materials. Preprint at <http://arXiv.org/abs/1411.0005> (2014).
12. Feng, J. *et al.* Large linear magnetoresistance in Dirac semi-metal Cd_3As_2 with Fermi surfaces close to the Dirac points. Preprint at <http://arXiv.org/abs/1405.6611> (2014).
13. Zhang, S. *et al.* Breakdown of Three-dimensional Dirac Semimetal State in pressurized Cd_3As_2 . Preprint at <http://arXiv.org/abs/1410.3213> (2014).
14. Novoselov, K. S. *et al.* Two-dimensional gas of massless Dirac fermions in graphene. *Nature* **438**, 197-200 (2005).
15. Hasan, M. Z. & Kane, C. L. Colloquium: Topological insulators. *Rev. Mod. Phys.* **82**, 3045-3067 (2010).
16. Qi, X.-L. & Zhang, S.-C. Topological insulators and superconductors. *Rev. Mod. Phys.* **83**, 1057-1110 (2011).
17. Zhang, H. *et al.* Topological insulators in Bi_2Se_3 , Bi_2Te_3 and Sb_2Te_3 with a single Dirac cone on the surface. *Nat. Phys.* **5**, 438-442 (2009).
18. Chen, Y. L. *et al.* Experimental Realization of a Three-Dimensional Topological Insulator, Bi_2Te_3 .

Science **325**, 178-181 (2009).

19. Zhao, Y. *et al.* Crossover from 3D to 2D Quantum Transport in Bi₂Se₃/In₂Se₃ Superlattices. *Nano Lett.* **14**, 5244-5249 (2014).
20. Yang, B.-J. & Nagaosa, N. Classification of stable three-dimensional Dirac semimetals with nontrivial topology. Preprint at <http://arXiv.org/abs/1404.0754> (2014).
21. Yi, H. *et al.* Evidence of Topological Surface State in Three-Dimensional Dirac Semimetal Cd₃As₂. *Sci. Rep.* **4**, 6106 (2014).
22. Ali, M. N., Gibson, Q., Jeon, S., Zhou, B. B., Yazdani, A. & Cava, R. J. The Crystal and Electronic Structures of Cd₃As₂, the Three-Dimensional Electronic Analogue of Graphene. *Inorg. Chem.* **53**, 4062-4067 (2014).
23. Qu, D. X., Hor, Y. S., Xiong, J., Cava, R. J. & Ong, N. P. Quantum Oscillations and Hall Anomaly of Surface States in the Topological Insulator Bi₂Te₃. *Science* **329**, 821-824 (2010).
24. Murakawa, H. *et al.* Detection of Berry's Phase in a Bulk Rashba Semiconductor. *Science* **342**, 1490-1493 (2013).
25. Bell, C. *et al.* Shubnikov-de Haas oscillations in the bulk Rashba semiconductor BiTeI. *Phys. Rev. B* **87**, 081109 (2013).
26. Novak, M., Sasaki, S., Segawa, K. & Ando, Y. Large linear magnetoresistance in the Dirac semimetal TlBiSSe. Preprint at <http://arXiv.org/abs/1408.2183> (2014).
27. Abrikosov, A. A. Fundamentals of the Theory of Metals. **1**. Amsterdam: North-Holland (1988).

Acknowledgments

We acknowledge Chong Wang and Yuan Li for the help in Laue measurements and thank Liang Li and Zhengcai Xia for helpful discussions about the pulsed magnetic field measurements. This work was financially supported by National Basic Research Program of China (Grant Nos. 2013CB934600 and 2012CB921300), the National Natural Science Foundation of China (Nos. 11222434, 11174007), and the Research Fund for the Doctoral Program of Higher Education (RFDP) of China.

Author contribution statement

J.W., S.J. and X.C.X. conceived and designed the study. Y.Z., H.W., Y.X. and J.W. made transport measurement experiments. J.F.W. and Z.L. helped in pulsed magnetic field measurements. C.Z., H.L. and S.J. grew the samples. J.L. and Y.W. made TEM study. H.L. and X.C.X. contributed to the theoretical explanation. Y.Z., H.L., and J.W. wrote the manuscript with input from all authors.

Additional information

Competing financial interests: The authors declare no competing financial interests.

Supplementary Information

Anomalous Quantum Oscillations in 3D Dirac Semimetal Cd₃As₂ Induced by 3D Nested Anisotropic Fermi Surface

Yanfei Zhao^{1,2,#}, Haiwen Liu^{1,2,#}, Chenglong Zhang^{1,2}, Huichao Wang^{1,2}, Junfeng Wang³, Ziquan Lin³, Ying Xing^{1,2}, Hong Lu^{1,2}, Jun Liu⁴, Yong Wang⁴, Shuang Jia^{1,2,*}, X. C. Xie^{1,2,*} and Jian Wang^{1,2,*}

¹International Center for Quantum Materials, School of Physics, Peking University, Beijing 100871, China

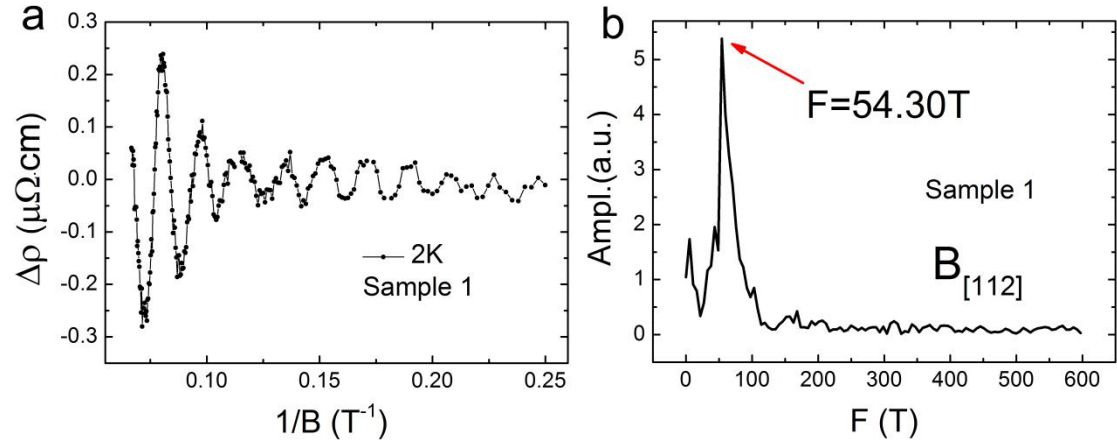
²Collaborative Innovation Center of Quantum Matter, Beijing 100871, China

³Wuhan National High Magnetic Field Center, Huazhong University of Science and Technology, Wuhan 430074, China

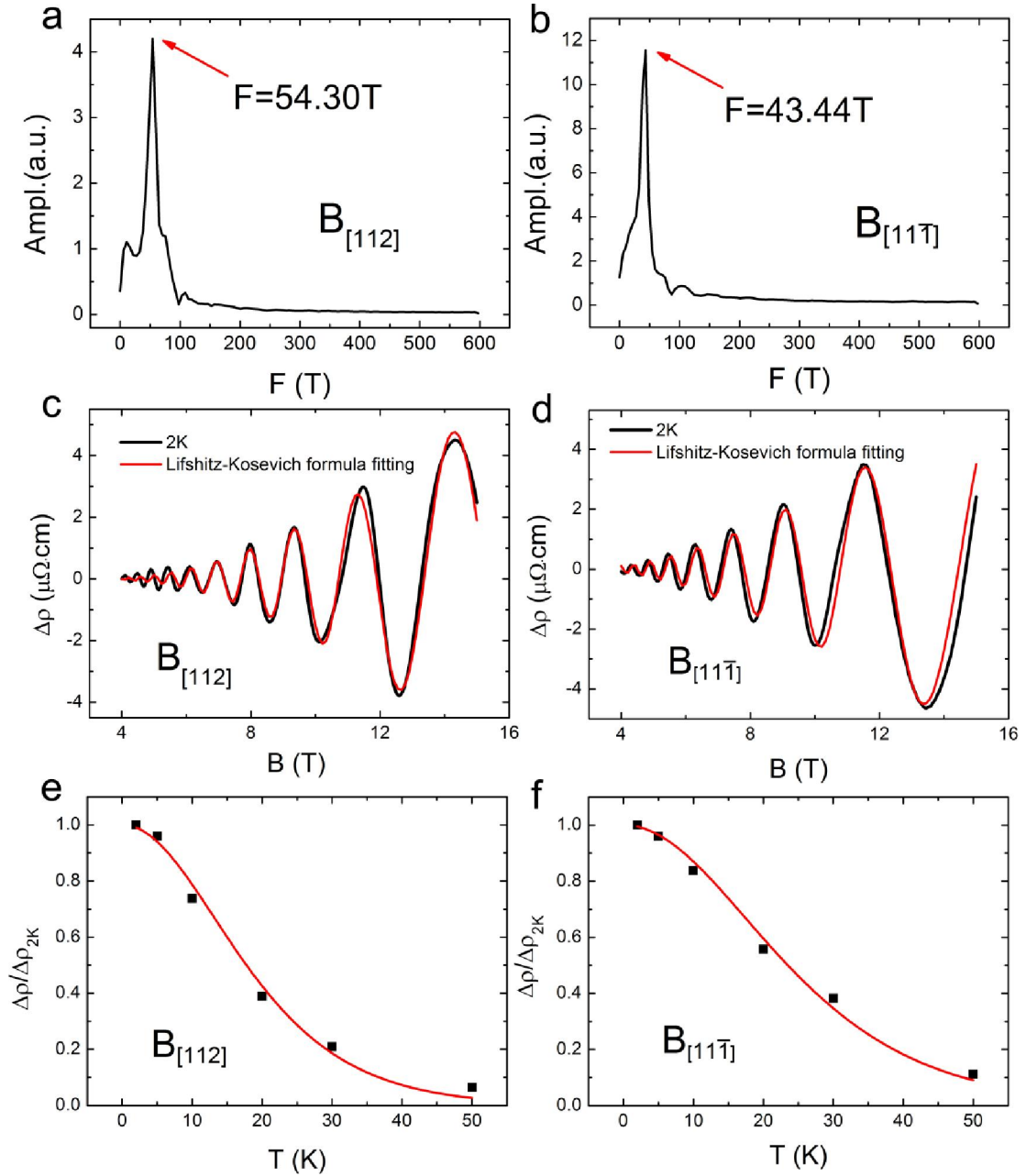
⁴Center of Electron Microscopy, State Key Laboratory of Silicon Materials, Department of Materials Science and Engineering, Zhejiang University, Hangzhou, 310027, China

[#] Authors equally contributed to this work.

Correspondence and requests for materials should be addressed to jianwangphysics@pku.edu.cn (J.W.), xcxie@pku.edu.cn (X.C.X.), gwljiashuang@pku.edu.cn (S.J.).

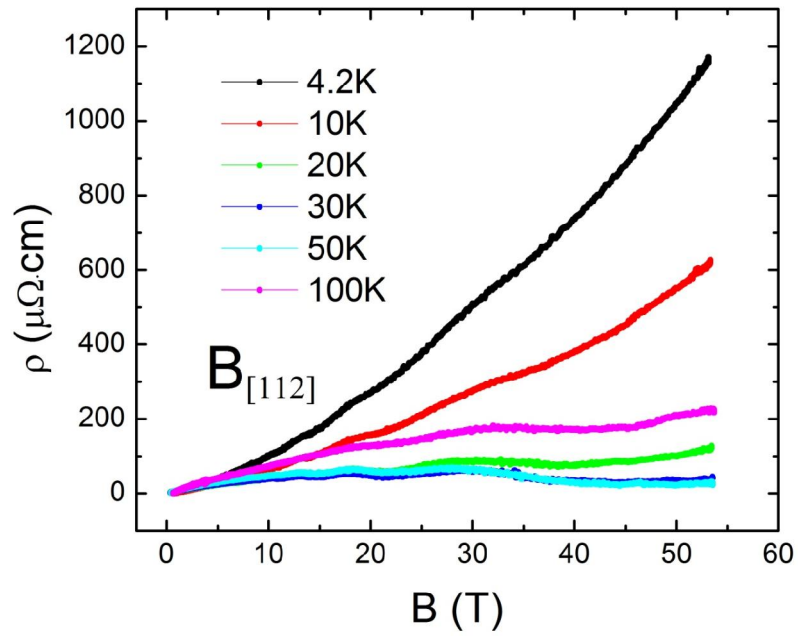


Supplementary Figure S1: Quantum oscillations in Sample 1 at $B_{[112]}$ direction. (a) After subtracting the nonoscillating background deduced by fitting a fourth-order polynomial, the oscillatory component $\Delta\rho$ as a function of $1/B$ at $T = 2$ K. Compared with the oscillations in sample 2, the amplitude of the oscillation here is smaller. (b) FFT analysis obtain a single frequency $F = 54.30\text{T}$, same as the frequency measured in sample 2.



Supplementary Figure S2: SdH oscillations analysis in $B_{[112]}$ and $B_{[11\bar{1}]}$ directions. (a)-(b) The frequency of the SdH oscillations was extracted from the fast Fourier transform (FFT) analysis. Single frequency was observed in both $B_{[112]}$ and $B_{[11\bar{1}]}$ directions. $B_{F[112]} = 54.30$ T and $B_{F[11\bar{1}]} = 43.44$ T. (c)-(d) shows the fitting to the entire oscillatory component with the standard Lifshitz – Kosevich (LK) theory for a 3D system in $B_{[112]}$ and $B_{[11\bar{1}]}$ directions respectively. The red solid line is the reasonable close fit to the observed oscillations (the black solid line) by the LK expression with a single frequency. (e)-(f) Plotted is the relative amplitude of oscillation $\Delta\rho/\rho_{2K}$ as a function of temperature for the Landau Level located at $n = 7$ marked in the maintext Figure 2 in $B_{[112]}$ and $B_{[11\bar{1}]}$ direction, respectively. By fitting the curve, we subtract the cyclotron effective mass $m_{[112]}^*$ =

$0.043 m_e$ and $m_{[11\bar{1}]}^* = 0.036 m_e$ (m_e is the free electron mass).



Supplementary Figure S3: Magnetotransport measured in Pulsed High Magnetic Field. Figure displays the magnetoresistance behavior measured in pulsed high magnetic field normal to the (112) plane up to 54 T at various temperatures.

The anisotropic Fermi surface and estimation of carrier density

We calculate the Fermi momentum using Weyl Hamiltonian: $H(\vec{k}) = \sum_{i=x,y,z} v_i \sigma_i k_i$ based on the SdH oscillation data. Due to the C4 symmetry in X-Y plane and anisotropic SdH oscillation period in $[112]$ and $[11\bar{1}]$ direction, the velocity satisfies $v_x = v_y \neq v_z$ and $k_x = k_y \neq k_z$. Based on the SdH period $S_{F[112]} = 54.30$ T and $S_{F[11\bar{1}]} = 43.44$ T for $B_{[112]}$ and $B_{[11\bar{1}]}$ direction, we calculate the momentum $k_x = k_y = k_{para} = 0.034 \text{ \AA}^{-1}$ and $k_z = 0.075 \text{ \AA}^{-1}$, and thus find Fermi velocity $v_x = v_y = 2.2 * v_z$. For the $B_{[1\bar{1}0]}$ direction case, the small period $F_1 = 43.44$ T and $k_{para} = 0.034 \text{ \AA}^{-1}$ give out the half major axis value $k_1 = 0.041 \text{ \AA}^{-1}$ for red (or blue) ellipse in Figure 5d of the main text. From the analysis of two periods behavior in $B_{[1\bar{1}0]}$ direction, the Dirac point location is deduced to be $(0, 0, \pm k_0)$. Considering $k_z = 0.075 \text{ \AA}^{-1}$ and $k_1 = 0.041 \text{ \AA}^{-1}$, one can estimate the location of Dirac point K (K') = $(0, 0, \pm k_0)$, with $k_0 = 0.058 \text{ \AA}^{-1}$. Moreover, we give out the orientation range of the nested ellipses region as shown by purple dashed line in Figure 5d. From $k_z = 0.075 \text{ \AA}^{-1}$ and $k_1 = 0.058 \text{ \AA}^{-1}$, we calculate the orientation range is about $[-21^\circ, 21^\circ]$, which is qualitatively consistent with the angle range with double periods features. The little deviation in the orientation range may attribute to the deformation of energy bands in the overlapping region. This deformation of energy bands around the Lifshitz saddle point might influence the Fermi velocity. From the momentum $k_x = k_y = 0.034 \text{ \AA}^{-1}$ and $k_z = 0.075 \text{ \AA}^{-1}$, we estimated the carrier density from two Dirac pockets to $n = 5.86 \times 10^{18} \text{ cm}^{-3}$.